Angular Momentum Budget in General Circulation Models of Superrotating Atmospheres: A Critical Diagnostic

Sébastien Lebonnois[1]
Curt Covey[2]
Allen Grossman[2]
Helen Parish[3]
Gerald Schubert[3]
Richard Walterscheid[4]
Peter Lauritzen[5]
Christiane Jablonowski[6]

Abstract.
To help understand the large disparity in the results of circulation modeling for the atmospheres of Titan and Venus, where the whole atmosphere rotates faster than the surface (superrotation), the atmospheric angular momentum budget is detailed for two General Circulation Models (GCMs). The LMD GCM is tested for both Venus (with simplified and with more realistic physical forcings) and Titan (realistic physical forcings). The Community Atmosphere Model is tested for both Earth and Venus with simplified physical forcings. These analyses demonstrate that errors related to atmospheric angular momentum conservation are significant, especially for Venus when the physical forcings are simplified. Unphysical residuals that have to be balanced by surface friction and mountain torques therefore affect the overall circulation. The presence of topography increases exchanges of angular momentum between surface and atmosphere, reducing the impact of these numerical errors. The behavior of GCM dynamical cores with regard to angular momentum conservation under Venus conditions provides an explanation of why recent GCMs predict dissimilar results despite identical thermal forcing. The present study illustrates the need for careful and detailed analysis of the angular momentum budget for any GCM used to simulate superrotating atmospheres.

1. Introduction

Numerical simulation of the superrotating atmospheres of Venus and Titan has long been a challenge. Superrotation is present when the total atmospheric angular momentum (AAM) referred to the rotation axis of the planet is larger than the angular momentum the atmosphere would have if it was at rest (no wind relative to the surface). It is directly related to the zonal wind field u, the component of the wind that is tangent to latitude circles. Many General Circulation Models (GCMs) of Venus and Titan have reached superrotation, starting from rest, but few have obtained satisfactory agreement with the strong superrotation observed in their atmospheres.

The accuracy of AAM conservation in Earth GCMs has occasionally been studied, e.g. by *Boer* [1990] for the Canadian Climate Center model and by *Lejenäs et al.* [1997] for the US Community Climate Model (CCM). Both studies find that friction and mountain torques account for the simulated AAM variations with very good precision. The CCM is an ancestor of the Community Atmosphere Model (CAM) used for some of the work discussed in this paper. For strongly superrotating atmospheres, several studies indicate the importance of a GCM's angular momentum conservation for producing satisfactory simulations. In the first work to successfully simulate the superrotation in Titan's atmosphere [*Hourdin et al.*, 1995], the authors acknowledge the importance of angular momentum conservation in the GCM and indicate that in their study, seasonal as well as short-term fluctuations of AAM are very close to that computed from the friction torque. Experiments by *Del Genio and Zhou* [1996] using the GISS GCM adapted for rotation rates of Titan and Venus have also indicated the need for accurate angular momentum conservation. Using single or double precision in their computations made a significant difference in the modeled circulations, especially in the case of a Venus-like rotation rate. More recently, *Newman et al.* [2011] have shown that the horizontal dissipation parameterization in the TitanWRF GCM has a strong influence on its ability to spin up Titan's atmospheric circulation.

In recent Venus GCMs, different conclusions were drawn concerning the role of topography, first introduced in *Hernstein and Dowling* [2007]. A comparative study of Venus GCMs in simplified configurations has been carried out by a working group of the International Space Science Institute (ISSI) in Bern, Switzerland [*Lebonnois et al.*, 2012b]. A precursor comparative study was done by *Lee and Richardson*

[1]Laboratoire de Météorologie Dynamique (LMD), IPSL, CNRS-UPMC (UMR 8539), Paris, France
[2]Lawrence Livermore National Laboratory, Livermore, CA, USA
[3]UCLA, Los Angeles, CA, USA
[4]Space Science Applications Laboratory, The Aerospace Corporation, M2-260, Los Angeles, CA, USA
[5]National Center for Atmospheric Research, Boulder, CO, USA
[6]Univ. of Michigan, Ann Arbor, MI, USA

0148-0227/12/$9.00

[2010]. These studies illustrate the wide disparity in results obtained with similar Venus GCMs forced with the same physical parameterizations. All the above work shows how sensitive the circulations in the atmospheres of Venus and Titan are to the numerics in dynamical cores of GCMs.

In this paper, we address the issue of angular momentum conservation in GCMs we have used to simulate the atmospheres of Venus, Earth and Titan. The total AAM of an atmosphere M is given by

$$M = M_o + M_r = \int_S \Omega a^2 \cos^2\theta \frac{p_s}{g} dS + \int_V ua\cos\theta dm, \quad (1)$$

where Ω is the rotation rate of the planet, a is its radius, g is its surface gravity, θ is latitude, p_s is surface pressure, u is the zonal wind, $\int_V dm$ is the integral of mass over the volume of the atmosphere, and $\int_S dS$ is the integral over the surface of the planet. The first term M_o is due to the solid body rotation of the planet (o stands for "omega") and the second term M_r is due to the movement of the atmosphere relative to the surface (r stands for "relative"). Hydrostatic equilibrium is used here, as well as the approximations that are present in the GCMs equations (shallow and spherical atmospheres). The model top is taken at $p = 0$ Pa. M_o and M_r are computed in the GCM simulations with discretized sums over the grid cells, with $\Delta S = a^2 \cos\theta \Delta\lambda \Delta\theta$ (where λ is the longitude) and $\Delta m = |\Delta p|/g \times \Delta S$.

In any GCM, the way the AAM evolves during a simulation can be divided into several components. The temporal evolution of the AAM is related to variations in the distribution of the mass at the surface (dp_s/dt, yielding dM_o/dt) or to variations of the zonal wind speed (du/dt, yielding dM_r/dt). Changes of M arise from exchanges of momentum at the surface and at the model's upper boundary, and to conservation errors within the GCM:

$$\frac{dM}{dt} = \frac{dM_o}{dt} + \frac{dM_r}{dt} = F + T + S + D + \epsilon, \quad (2)$$

where F is the total angular momentum tendency from the boundary layer scheme (friction near the surface), T is the rate of exchange of AAM with the surface due to surface pressure variations, related to topographical features (mountain torque), S is the total angular momentum tendency due to upper boundary conditions (e.g., a sponge layer), D is a residual torque due to conservation errors in the parameterization of horizontal dissipation, and ϵ is a residual numerical rate of angular momentum variation due to other conservation errors. In the usual GCM configuration, the physical parameterizations are separated from the dynamical core. The S and D terms are part of the dynamical core though S may be in the physical package in some GCMs.

To get an estimate of ϵ in a GCM simulation, the different variables in Eq. (2) need to be computed. Some contributions to the AAM are easy to isolate. In the GCMs used for this study, the only contribution to zonal wind variations computed in the physical package arises in the planetary boundary layer scheme (friction near the surface) $\left(\frac{du}{dt}\right)_F$. From this tendency, F can be computed from

$$F = \int_V a\cos\theta \left(\frac{du}{dt}\right)_F dm. \quad (3)$$

The total contribution from the dynamical core (dycore) to variations in the zonal wind can be obtained at runtime by computing the change in zonal wind between the end of one call to the physical package and the start of the next call. This contribution $\left(\frac{du}{dt}\right)_{dyn}$ includes all variations of u occuring in the dynamics. From this tendency, the associated torque Dy can be computed as

$$Dy = \int_V a\cos\theta \left(\frac{du}{dt}\right)_{dyn} dm. \quad (4)$$

The evolution of the relative atmospheric angular momentum M_r can then be written as

$$\frac{dM_r}{dt} = F + Dy. \quad (5)$$

The mountain torque T is included in Dy but can also be evaluated separately. Any resolved wave forced by the orography induces surface pressure variations that will then produce a drag through the mountain torque. The mountain torque results from pressure forces from the surface on the atmosphere:

$$\vec{T} = \int_S p_s \vec{r} \times \vec{n} ds$$

where $\vec{n}$ is the unit vector normal to the surface, and ds is the actual surface element. In the spherical referential $(\vec{e_r}, \vec{e_\lambda}, \vec{e_\theta})$, $\vec{n}ds$ coordinates are $dS \times (1, -\frac{1}{a\cos\theta}\frac{\partial z_s}{\partial\lambda}, -\frac{1}{a}\frac{\partial z_s}{\partial\theta})$, where z_s is the topographic height and $dS = a^2\cos\theta d\lambda d\theta$ is the horizontal surface element. Therefore, given the approximation $\vec{r} = a\vec{e_r}$, we have

$$\vec{T} = \int_S a p_s \left(\frac{1}{a}\frac{\partial z_s}{\partial\theta}\vec{e_\lambda} - \frac{1}{a\cos\theta}\frac{\partial z_s}{\partial\lambda}\vec{e_\theta}\right) dS$$

and projected on the rotation axis $\vec{k}$ ($\vec{e_\lambda} \bullet \vec{k} = 0, \vec{e_\theta} \bullet \vec{k} = \cos\theta$):

$$T = -\int_S p_s \frac{\partial z_s}{\partial\lambda} dS. \quad (6)$$

Subgrid scale gravity waves may also produce an additional drag, but it needs to be parameterized in the physical package to be present and taken into account in the GCMs. An additional term is then added to F. This is not the case in our simulations.

Using Eq. (5) in Eq. (2) and then solving for $S + D + \epsilon$, the unphysical contribution to the simulated AAM can be estimated from

$$\epsilon^* \equiv S + D + \epsilon = Dy - T + dM_o/dt, \quad (7)$$

where the three terms on the right side are evaluated from Eqs. (4), (6) and the time derivative of the M_o part of Eq. (1). The integrals are evaluated by summing over the GCM's grid cells. When the tendencies $\left(\frac{du}{dt}\right)_S$ and $\left(\frac{du}{dt}\right)_D$ can be obtained from the dycore during a GCM simulation run, S and D can be computed individually. However, in some cases it is not possible to easily extract these tendencies due to the structure of the dycore.

In this work, the sources and sinks of AAM variations, including unphysical contributions, are estimated for two different GCMs: the LMD GCM, in its Venus [*Lebonnois et al.*, 2010] and Titan [*Lebonnois et al.*, 2012a] configurations, and the Community Atmosphere Model, in its Venus [*Parish et al.*, 2011] and simplified Earth [*Held and Suarez*, 1994] configurations. These models and the simulations done for this study are described in Section 2. In Section 3, contributions to the AAM variations are illustrated, and consequences of unphysical sources and sinks for the circulation

are discussed, especially with regard to the superrotation question.

2. LMD and CAM General Circulation Models

2.1. LMD Models and Simulations

Venus LMD GCM: This model is used in a configuration similar to the one described in *Lebonnois et al.* [2010] and denoted by LEB10 below. The dycore is a finite-difference scheme and takes into account the specific heat as a function of temperature. A digital longitudinal filter is applied poleward of 60° latitude to limit the effective resolution to that at 60° latitude. Horizontal dissipation uses an iterated Laplacian, with the same time constants as LEB10. Horizontal resolution used is 48 longitudes and 32 latitudes, with and without topography, on 50 vertical levels. This coarse resolution is needed for computational cost, because this version of the LMD GCM can run on only one processor (no parallelization yet). Compared to LEB10, the most noticeable change is the planetary boundary layer (PBL) scheme. The GCM now includes a "Mellor and Yamada" parameterization [*Mellor and Yamada*, 1982], taken from the Earth version of the LMD GCM and fully described in the Appendix B of *Hourdin et al.* [2002]. This new boundary layer scheme modifies significantly the temperature and wind profiles in the deep atmosphere between the surface and the cloud base. The initial states used were taken from previous stable states run from rest for several hundred Venus days (Vd, synodic, equal to 116.7 Earth days or 1.008×10^7 s). Simulations were run for an additional 50 Vd and are labelled LMDFN and LMDFT, where F stands for "Full physics", N for "No topography" and T for "Topography".

Simplified Venus LMD GCM (ISSI configuration): Described in *Lebonnois et al.* [2012b], this configuration includes simple surface friction and simple temperature forcing [based on works by *Lee*, 2006; *Lee et al.*, 2007] instead of full physics. In this case, the dycore takes into account a fixed specific heat ($C_p = 900J/kg/K$) and the same horizontal resolution as LMDF* simulations is used for the simulations labelled LMDIN and LMDIT (where I stands for "Idealized physics"). These simulations were started from rest, and run for 400 Vd.

Titan LMD GCM: This model is described in *Lebonnois et al.* [2012a]. The dycore is the same as for Venus (albeit with constant specific heat). Horizontal resolution used is 32 longitudes and 48 latitudes, on 55 vertical levels. Here, no topography is taken into account. Radiative transfer includes diurnal and seasonal cycles. The simulation shown in *Lebonnois et al.* [2012a] is used, covering one Titan year (equivalent to roughly 90 Vd), and labelled TITAN.

In the LMD GCM dycore, it is possible to isolate the tendencies due to the horizontal dissipation and to the sponge layer and output $\left(\frac{du}{dt}\right)_S$ and $\left(\frac{du}{dt}\right)_D$ during the simulation runs. Therefore, S, D and ϵ can be separated.

2.2. CAM Models and Simulations

Venus CAM GCM: This model is described in *Parish et al.* [2011]. However, while *Parish et al.* [2011] used CAM3 [*Collins et al.*, 2004; *Collins et al.*, 2006], we use CAM5 [*Neale et al.*, 2010], with notable changes in the horizontal dissipation scheme compared with CAM3's Laplacian damping. Horizontal dissipation options in CAM5 are: second order divergence damping (which includes a feature acting as a sponge layer at the top of the model), and fourth order divergence damping with or without an additional Laplacian damping at the top of the model which acts as a sponge layer [*Jablonowski and Williamson*, 2011; *Whitehead et al.*, 2011; *Lauritzen et al.*, 2012]. Without the Laplacian damping explicitely added, the fourth order divergence damping option still invokes an implicit numerical sponge layer, because of the degradation of the numerical scheme from third-order to first-order near the top of the model. The dycore is a finite-volume scheme [CAM-FV, *Lin*, 2004] with horizontal resolution $1.25^\circ \times 0.9^\circ$ (288 longitudes and 192 latitudes). The code can run in parallel on many processors (typically 192), allowing high horizontal resolution. The vertical grid is the same as the LMD Venus GCM grid, on 50 levels. A Fast Fourier Transform (FFT) longitudinal polar filter is applied poleward of the midlatitudes. This model includes simplified physics and constant specific heat as in the ISSI configuration of the LMD model, so the simulation labels start with I. Simulations are done with (label IT*) and without (label IN*) topography, for roughly 150 Vd. The different horizontal dissipation options are used and indicated in the simulation label (2 for second order, 4 for fourth order without an explicit Laplacian sponge layer and 42 for fourth order with the Laplacian sponge layer). The dissipation is used either with its default coefficient (S, for "Standard") or with a coefficient reduced by a given factor (e.g., R10 for "Reduced by 1/10"). In most cases, the initial state was taken from the *Parish et al.* [2011] simulations. Some simulations were also started from rest (labelled I0* instead of I*) and run for 300 Vd without topography (I0N42R10), and 100 Vd with topography (I0T42R10).

Earth CAM GCM: The Earth version for CAM5 was also used in the present work in its Held-Suarez configuration, i.e., without topography, with a simple Newtonian temperature relaxation and Rayleigh friction near the surface, exactly as described in *Held and Suarez* [1994] (idealized physics in the Venus GCMs described above are slight variations of the Held-Suarez procedure). The horizontal resolution used is the same as for Venus, on 26 vertical levels. The different horizontal dissipation options were tested and the simulations (labelled EIN*) were run for 10 Earth years, though only the last year is discussed below.

Due to some complexities in the CAM finite volume dycore, it has not been possible for us to separate S and D from ϵ.

3. Analysis of Angular Momentum Budgets

3.1. Elements for the Analysis

Table 1

For each simulation (summarized in Table 1), we computed M, its temporal variation dM/dt (as well as dM_o/dt and dM_r/dt), the different torques F, Dy, T, ϵ^* (in the case of the CAM GCM) or D, S and ϵ (in the case of the LMD GCM). The sum of all torques $\Sigma = F + Dy$ was also computed as a check compared to dM_r/dt. These time series are shown below in Figs. 1 to 7.

Table 2

Table 2 shows the temporal average values of these torques for all the simulations. Time averages are done over the whole simulation. Given the variability of each variable (depending on the simulation), the time average (indicated with an overbar) may vary slightly as a function of the time series taken into account, especially when the average is much lower than the amplitude of the variations. Only $\overline{dM_r/dt}$ is shown, as $\overline{dM_o/dt}$ is 5 orders of magnitude smaller in the case of Venus, 4 orders of magnitude smaller for Titan, and 3 orders of magnitude smaller for the Earth. For the Earth simulations, $\overline{dM_r/dt}$ is significantly more different from $\overline{\Sigma}$ than for Venus or Titan. This is possibly due to the different output schedules for the different variables

(u, p_s used to compute the mass, $(du/dt)_{dyn}$ and $(du/dt)_F$), in a situation where temporal variations of the mass are not negligible (dM_o/dt is not negligible, as it is for Venus and Titan). Table 2 illustrates the average balance between the different torques. In steady state $\overline{dM_r/dt}$ should be zero, but taking into account that each simulation starts with some adjustment phase, this is never the case in practice, especially when the circulation undergoes oscillations.

Table 3

Table 2 shows that $\overline{\epsilon^*}$ is always a significant part of $\overline{dM_r/dt}$, but because $\overline{dM_r/dt}$ is expected to be a small residual of competing effects, the global area-average balance is not enough to fully describe the impact of ϵ^* on the AAM budget. At the surface, mountain and friction torques are positive (upward momentum transfer) in some locations (T^+, F^+) and negative in others (T^-, F^-). The maximum amplitudes of these competitive transfers can be compared to $\overline{\epsilon^*}$, to see whether this non-physical term can affect the balance in the surface exchanges. Therefore, Table 3 presents the temporal average values of these quantities, as well as the ratio

$$\xi = \frac{|\epsilon^*|}{Max\left(\overline{T^+} + \overline{F^+}, |\overline{T^-} + \overline{F^-}|\right)}. \quad (8)$$

This parameter ξ can be interpreted as an indication of the relative perturbation caused by ϵ^* in the surface balance of angular momentum.

Table 4

All variables that are used in the analysis in the Sections below are summarized in Table 4 for easy reference.

3.2. Venus LMD

Fig. 1

Spin-up in the LMDI* simulations: Figure 1 shows the evolution of the total angular momentum as well as the different torques during the spin-up of simulations LMDIN and LMDIT. Except for the resolution used, these simulations are very similar to the simulations run with the LMD GCM for the ISSI intercomparison work [*Lebonnois et al.*, 2012b]. However, the results appear surprisingly different. The spin-up phase is longer here and the total angular momentum M (linked to the circulation, though more sensitive to the deeper atmosphere) does not stabilize during these 400 Vd. As can be seen in Fig. 1, in both N and T cases, the friction and the mountain torques are initiating the circulation, but after 10 Vd, the amplitude and variability of the dynamical term ϵ increases and perturbs the angular momentum budget. The horizontal dissipation and upper sponge layer are negligible in the budget. The amplitude of ϵ variations as well as $\overline{\epsilon}$ are comparable to the physical forcings F and T. The ratio ξ shows that topography increases the surface exchanges and reduces ξ to a very small value. However, ξ is an averaged value, and Fig. 1 illustrates how much it may vary with time.

Discussing the modeled circulation is not the point of this paper, but the high sensitivity of this circulation to tiny details in the GCM needs to be emphasized and kept in mind. After more than 300 Vd, winds have reached Venus-like values at most levels, and ϵ increases in amplitude and average value, inducing a decrease in total AAM. The same behavior is obtained with or without topography. This impact of $\overline{\epsilon}$ will be discussed more extensively below in the context of the ISSI intercomparison study, with the additional example of the CAM GCM.

Fig. 2

Dycore perturbations in the LMDF* simulations: The simulations LMDFN and LMDFT, based on realistic physics, are reported in Fig. 2. Only six days are shown to clearly see the diurnal cycle and increase readabiliy. These simulations are comparable to the simulations presented in LEB10. For the angular momentum budget, see in particular Figs. 1 and 2 and Table 3 in that work. As in LEB10, D and S are negligible, but this is not the case for ϵ. In LEB10, $\overline{\epsilon}$ was compensated by the average $\overline{T}$ (topography run) or $\overline{F}$ (no-topography run). Here, in the no-topography case, $\overline{F}$ does not compensate $\overline{\epsilon}$ and the momentum is slightly drifting downward. In the topography case, $\overline{F}$ compensates $\overline{\epsilon}$, which is different from LEB10, where this compensation was coming from $\overline{T}$. The oscillations seen are from the diurnal cycle, similar to the ones seen in LEB10 (with less temporal resolution).

These differences between the simulations in LEB10 and those presented here are due to the boundary layer scheme, which affects the stability structure close to the surface and the angular momentum in the deep atmosphere, and also to the duration of the runs, since reaching circulation stability takes a very long run time in this case. The superrotation factor (defined here as the ratio between the total AAM M and its solid body rotation part M_o) is around 2.7 (this work) instead of 1.4 (LEB10) in the case with topography (due to higher winds in the deep atmosphere, below the clouds). Without topography, it goes down to 0.7 (this work) instead of 0.9 (LEB10). It is also seen in LEB10 (Fig. 1) that after an initial spin-up, the case without topography loses angular momentum, as it does here, then stabilizes.

From LMDIN to LMDFT: reducing the influence of ϵ^*: Compared to the idealized simulations LMDI*, the amplitude of the variations of ϵ are much smaller in the LMDF* cases, though the overall impact of ϵ is not significantly improved. However, the more realistic PBL and radiative schemes are more efficient at stabilizing the circulation. When topography is present, the diurnal cycle clearly dominates the variability both for T and F, with amplitudes much larger than the variability of ϵ. Again, the presence of the mountain torque significantly reduces the impact of ϵ on the overall AAM budget. Comparing LMDFT and LMDIT, the value of ξ appears slightly larger in LMDFT than in LMDIT. However, it must be noted that the temporal average of ϵ^* includes values that change sign during the long simulation done for LMDIT, while ϵ^* is stable for LMDFT.

3.3. Venus CAM

Fig. 3

IN*S: role of ϵ^* in the absence of topography: From Table 3, it is clear that without topography, ϵ^* is generally greater than positive and negative surface torques, and dominates completely the evolution of M in all cases. The ξ parameter clearly indicates a non-physical perturbation much stronger than the surface exchanges. Changing the horizontal dissipation scheme to fourth order does not improve the situation much. The amplitude of ϵ^* is higher in IN4S compared to IN2S (not shown) but its temporal average $\overline{\epsilon^*}$ is lower in steady state.

IT*S: large $\overline{\epsilon^*}$ compensated by mountain torque: In the IT2S simulation, $\overline{T}$ compensates $\overline{\epsilon^*}$, but these values are very large compared to the variability of dM/dt. In the IT4S simulation, oscillations are visible once the transition phase is over. This behaviour is qualitatively different from the IT2S run. As in IT2S, variations of T and ϵ^* are comparable and on average $\overline{T}$ compensates $\overline{\epsilon^*}$ but their signs are reversed compared to IT2S. The addition of topography

increases the surface exchanges by two orders of magnitude, significantly reducing the potential impact of ϵ^* on the AAM budget.

Fig. 4

Reducing the horizontal dissipation: For the CAM5 runs, reducing the coefficient used in the divergence damping from the standard values used in Earth simulations [as detailed in *Lauritzen et al.*, 2012] was tested to evaluate the impact of D within ϵ^*. However, when the 2nd order divergence damping coefficient is reduced by a factor of 10, the simulation becomes unstable. Reducing it only slightly does not make a significant difference. Stability issues of the divergence damping mechanism in CAM-FV are discussed in *Whitehead et al.* [2011].

In the case of 4th order divergence damping, the coefficient was reduced using factors of 1/10 and 1/30. With topography, the impact of reducing the horizontal dissipation is obvious from the ϵ^* torque (Fig. 4), and the very low values obtained for ξ also reflects this improvement. Without topography, the effects of reducing the horizontal dissipation are not directly visible in the torque or in the ξ ratio, but some improvement is visible in the evolution of M (not shown). In the IT4R* runs, the mountain torque T dominates the variations of M, and the same oscillations as for the IT4S run are visible. The amplitude of the ϵ^* torque is reduced when the 4th order divergence damping is reduced, but this improvement saturates when the reduction coefficient is less than 1/30 (not shown). As for the IT4S run, $\overline{T}$ and $\overline{\epsilon^*}$ balance on average after the initial transition phase. These values are significantly reduced when reducing the divergence damping coefficient, though this effect also saturates with further reduction of the coefficient.

Comparing I*4R10 with LMDI* simulations: These idealized simulations are similar to the LMDI* simulations. However, the amplitude of F is much smaller for the CAM simulations, while the amplitude of the temporal variations of ϵ^* as well as its temporal average are much larger. Though $\overline{\epsilon^*}$ and the amplitude of its variations have been reduced when reducing the divergence damping coefficient in the IT4R* simulations, they are still much larger than the values of ϵ^* in the corresponding LMDIT run. However, the ξ ratio is similar. The impact of resolution can be questioned, since both models are not at the same resolution, which certainly explains the different amplitude of the mountain torque surface exchanges. However, when reducing the resolution in CAM to a resolution of 72 longitudes and 46 latitudes, the situation is much worse: for simulations similar to IN4R10 and IT4R10, $\overline{\epsilon^*}$ is 10 to 70 times larger (of the order of 50×10^{18} kg m^2 s^{-2}, variations not shown here). The LMD GCM could not be run at higher resolution for this study due to computational times.

The oscillations in IT4R*: The oscillations seen in the M time series look similar to those discussed in *Parish et al.* [2011]. However, the *Parish et al.* [2011] simulations were run without topography. In the present simulations, no oscillations are present when there is no topography, but they appear in the simulations with topography. There are two hypotheses for these oscillations: whether they are related to some modes excited by the topography, or they are not physical, driven by some kind of interaction between T and ϵ^*. This second hypothesis is not supported by runs with reduced dissipation coefficient. However, this question is out of the scope of this paper and will be studied in future work dedicated to this simulation.

Fig. 5

Simulations started from rest: I0*42R10 - influence of ϵ^* in the spin-up: Adding the sponge layer at the top does not change much the simulations (with or without topography). This is compatible with a negligible contribution of S in the dynamical torque, as is the case for the LMD GCM.

When initially starting from rest (Fig. 5), simulations I0*42R10 reach a state close to simulations I*42R10 after some time (roughly 200 Vd for IN42R10, roughly 30 Vd for IT42R10). The simulation I0N42R10 is very similar to the basic case of the ISSI comparative study [*Lebonnois et al.*, 2012b], and can also be compared to the LMDIN simulation. In this case, it appears clearly that $\overline{\epsilon^*}$ dominates the AAM variations from the beginning, inducing a non-physical input of angular momentum that dominates dM/dt during the spin-up phase. The value of the F torque is always much smaller than in the LMDIN simulation.

When topography is included (simulation I0T42R10), the mountain torque is pumping momentum into the atmosphere during the spin-up phase, while the dynamics ($\overline{\epsilon^*}$) is slowing the spin-up. In this case, even though the dynamics term is not negligible, the mountain torque is really forcing the atmosphere to spin-up, as it is in the LMDIT simulation. The ξ ratio is very low both for LMDIT and I0T42R10 simulations. However, their temporal history is different, and these simulations have many other aspects that are very different (F amplitude, F vs T, circulation, total AAM, oscillations, etc...), illustrating again the extreme sensitivity of the circulation to the model used.

The role of ϵ^* demonstrated here gives a good explanation of the very large disparity obtained in the ISSI simulations: the behaviour of the dynamical core can dominate the surface friction and therefore control the total angular momentum budget. It is very different from one GCM to the other, and has a strong influence on the modeled circulation both during spin-up and once the circulation is stable. The mountain torque increases the amplitude of physical interactions with the surface, but even in this case, the dycore creates an artificial source (or sink) of AAM, impacts the AAM transport and affects the time when the GCM will reach steady state at the surface through friction and mountain torque balance.

3.4. Titan LMD

Fig. 6

The case of Titan's atmosphere simulated with the LMD GCM is illustrated in Fig. 6. Though the circulation is mostly stabilized, the total angular momentum is slightly increasing in this simulation (though only 0.8% per Titan year), indicating that global equilibrium is not yet completely reached. The detail of the torques shows that the friction with the surface follows a seasonal cycle, and compensates the losses of momentum due to the sponge layer, the horizontal dissipation and the residual dynamical term, all three of them being roughly the same order of magnitude. The ξ ratio of this average loss to the amplitude of surface momentum exchanges is small, though not negligible. This compensation certainly affects slightly the distribution and amplitude of winds at the surface, and also in the atmosphere through angular momentum transport.

Due to the lack of knowledge about Titan's topography, this GCM has not yet been run with topography. The impact of a first-approximation topography on the angular momentum budget has been recently studied by *Tokano* [2012] in the case of the Köln Titan GCM [*Tokano et al.*, 1999]. In these simulations, the dycore contribution was estimated and also shown to be non-negligible both without and with topography.

3.5. Earth CAM

Fig. 7

Finally, the case of Earth's atmosphere simulated with CAM is illustrated in Fig. 7. Recall that our Earth simulations follow the simplified physics prescription of *Held and Suarez* [1994]. This is similar to the idealized physics of VenusCAM and the other Venus models in *Lebonnois et al.* [2012b]. It does not include topography, and of course it forces the temperature field to values appropriate for Earth rather than Venus. In the following discussion we call this version of the model EarthCAM. Its time variations are shown in Fig. 7 in terms of local Earth days during the 10th Earth-year of three simulations, long after the model has reached a statistical steady state (although a time coordinate in days or years is arbitrary because the model lacks diurnal and seasonal cycles). As in previous time series figures, Fig. 7 shows total AAM ($M = M_o + M_r$; see Eq.(1)) on the left and torques on the right. The three simulations shown differ in the type of divergence damping employed (2nd vs. 4th order) and in the coefficient of 4th-order damping (standard [*Lauritzen et al.*, 2012] or one-tenth standard).

Variations of M in the EIN* simulations: Unlike Venus and Titan, Earth rotates rapidly and does not exhibit superrotation, therefore M_o ($=1.026 \times 10^{28}$ kg m^2 s^{-1} in our simulations) makes up nearly all of M. Using model output to compute the last term in Eq. (1) reveals that M_r in all three EarthCAM simulations is about 1.1×10^{26} kg m^2 s^{-1} (roughly 1% of M_o). This value is remarkably near the observed value 1.5×10^{26} kg m^2 s^{-1} [see Table 1 of *Egger et al.*, 2007] considering that EarthCAM's simplified physics omits mountain torque, an important part of the real atmosphere's angular momentum balance. All three EarthCAM simulations exhibit time variations of M around $\pm 0.1\%$ ($\pm 1 \times 10^{25}$ kg m^2 s^{-1}) over time scales of order one to 100 Earth-days. These variations of M are a combination of variations of M_o and M_r of the same order of magnitude. The relative variations of M_o are very small (0.1%), i.e. surface pressure, which is proportional to atmospheric mass per unit surface area, is constant to within a small tolerance. M_r in EarthCAM varies at about the 10% level, similar to the observed standard deviation of M_r [*Egger et al.*, 2007], though many forcings are not included in EarthCAM (diurnal and seasonal cycles, topography, the El Nino / Southern Oscillation and other forcings).

Balance between F and ϵ^* and their amplitude: The right side of Fig. 7 shows globally integrated torques in EarthCAM's three simulations. Since T is zero by construction, and time derivatives of M, M_o and M_r average to zero by definition in a statistical steady state, F and ϵ^* must approximately balance each other. Figure 7 and Table 2 show this balance with $F \sim +1 \times 10^{19}$ kg m^2 s^{-2} in EIN2S and EIN4S, rising to $+2 \times 10^{19}$ kg m^2 s^{-2} in EIN4R10, and ϵ^* equal and opposite on average (though more variable than F). These numbers are very similar to the variability of dM/dt, and are therefore not negligible (as seen in Fig. 7). Inter-comparison of the three simulations shows that reducing the influence of divergence damping by going to a higher order of damping or by reducing the damping coefficient does not reduce the magnitude of the unphysical ϵ^* terms in the angular momentum balance. We do find, however, that the magnitude of $\overline{\epsilon^*}$ is reduced as resolution is made finer: for the EIN2S simulation it decreases by about a factor of two each time the grid spacing is halved (result not shown). These results imply that the ϵ^* terms arise from discretization errors in the numerics rather than any unphysical formulation of the model's dissipation, since divergence damping – in contrast to Laplacian diffusion – does not introduce any spurious torque in the zonal momentum equation.

Values of ξ indicate a moderate perturbation of the dycore: As noted in Table 3, the globally integrated value of F shown in Fig. 7 is a residual of EarthCAM's larger torques at different latitudes. Examination of the zonal mean of F (not shown) reveals that the model simulates positive torque equatorward of about 30° North and South latitudes and negative torque at higher latitudes. This pattern agrees with theory and observations of Earth's atmosphere [e.g., Chapter 10 of *Holton*, 2004]. It provides confidence that the model is correctly simulating the fundamental features of the atmosphere's general circulation, despite the rather large fraction of the globally averaged angular momentum budget represented by nonphysical ϵ^* terms: $\xi \sim 10 - 20\%$. In this context it is noteworthy that the VenusCAM simulations including topography, 4th order divergence damping and a reduced damping coefficient (IT4R* in Table 3) achieve a more accurate angular momentum balance than our EarthCAM simulations: $\xi \sim 1 - 5\%$.

Potential sources of errors in CAM dycore: By analogy with the Venus results discussed above, the lack of mountain torque in EarthCAM may increase relative errors in the AAM budget by weakening the overall forcing. An ancestral version of CAM, the Community Climate Model (CCM), obtained smaller errors when mountain torque was included: *Lejenäs et al.* [1997] found a globally- and annually-averaged 'bias' of about 1×10^{18} kg m^2 s^{-2}, an order of magnitude less than ϵ^* for EarthCAM (Table 2). Identification of all sources of CAM's AAM conservation errors is beyond the scope of this paper, but noteworthy possibilities include a vertical remapping procedure that conserves total mass, energy and momentum but not angular momentum, and a shape-preserving filter in the advection operators included to control spurious grid-scale vorticity. Neither of these algorithms are included in the CCM's spectral dynamical core. Such algorithms can introduce numerical diffusion, and although real-world diffusion must conserve angular momentum, a model's diffusion – either deliberately introduced or implied by the numerics – need not conserve angular momentum. For example, because spherical harmonics are eigenfunctions of the horizontal Laplacian operator, the classic del-squared diffusion operator applied to a spherical harmonic component of the velocity field will simply multiply that component by a constant. Subsequent multiplication by $a\cos(\theta)$ and integration over horizontal area will in general produce a nonzero diffusion torque. However, in spectral transform models the Laplacian diffusion operation can be designed so that it does not damp uniform rotation [see, e.g., *Neale et al.*, 2010, section 3.3.14].

Oscillations compared for Earth and Venus CAM simulations: Another point of comparison between EarthCAM and VenusCAM involves the time oscillations of M. These are less spectacular in the VenusCAM results reported here than in the VenusCAM results reported by *Parish et al.* [2011]. They also occur at different periods: ~ 3 Earth-years as reported here vs. ~ 10 Earth-years in *Parish et al.* [2011]. The results reported here strongly suggest that VenusCAM's configuration in *Parish et al.* [2011], with no topography and strong Laplacian diffusion, produces an angular momentum balance dominated by unphysical ϵ^* terms. Nevertheless, we find substantial M oscillations in our more physical VenusCAM simulations, e.g., with $\sim 30\%$ peak-to-peak amplitude in IT4R30 after 30 Venus-days, when T and dM/dt are nearly equal and ϵ^* is relatively small (Fig.4). For EarthCAM, Fig. 7 shows that F and dM/dt are correlated but offset by the aforesaid $1 - 2 \times 10^{19}$ kg m^2 s^{-2}, which is of the same order of magnitude as their temporal variability. We conclude that unforced long period oscillations of zonal winds are physically plausible for Venus as well as Earth, and merit further investigation.

4. Discussion

The simulations presented in this study show how the LMD and CAM dycores affect the atmospheric angular momentum budget through non-physical angular momentum

residual sources and sinks. This is particularly problematic in the case of the superrotating atmospheres of Venus and Titan because superrotation is built through the imbalance between surface sources and sinks of AAM. Both terms may be much larger than the AAM conservation errors, but their difference, which is crucial for circulation build-up, is not. In the case of Mars or Earth, the processes controlling the circulation are less sensitive to angular momentum errors (and the associated compensation at the surface). The LMD model is shown to be more stable when the physical forcings (radiative transfer, planetary boundary layer scheme) are more realistic, with AAM and torques not varying much after several hundred Venus days and with a stable ϵ term. In the case of Venus, the topography induces stronger momentum exchanges with the surface and these simulations are therefore less sensitive to dycore residuals. The CAM model has larger non-physical terms, even at the high resolution used in this work. Their impact is reduced when the fourth-order divergence damping scheme is used for horizontal dissipation, with a coefficient reduced compared to the nominal Earth version. However, topography is needed to get strong enough surface exchanges to dominate dycore residuals. Its behaviour under realistic forcings remains to be tested.

This study illustrates that the way the dycore and the associated horizontal dissipation are implemented can significantly alter the atmospheric angular momentum budget, inducing non-physical contributions that have to be estimated to check the validity of GCM simulations. The mechanisms proposed to interpret superrotation development involve angular momentum transport and balance between mean meridional circulation and waves. Therefore, wave activity is a crucial aspect of the superrotation generation. The dycore AAM contributions are linked to grid-scale numerical conservation issues in the dycore schemes (filters, discretization schemes) that must affect wave propagation, interfering with the superrotation development. It affects the spin-up phase of superrotating atmospheres, the angular momentum budget everywhere in the atmosphere, and therefore its transport and global redistribution. The winds in the layers close to the surface are affected through the balance between sources and sinks in the friction and mountain torques, since the exchanges with the surface have to compensate for the numerical sources or losses of AAM.

Difficulties in the spin-up of superrotating atmospheres have been discussed previously for Titan with different GCMs, e.g., the Köln GCM [*Tokano et al.*, 1999], or a version of CAM adapted for Titan, but used at low horizontal resolution [*Friedson et al.*, 2009]. Issues related to the dycore were already pointed out in the case of the Titan-WRF GCM [*Richardson et al.*, 2007; *Newman et al.*, 2011]. For Venus, the ISSI study [*Lebonnois et al.*, 2012b] showed a wide disparity in simplified-forcing Venus GCM results, without investigating the reasons for these differences. The simulations performed in the current work allow us to conclude that this disparity is certainly related to the different behaviours of the dycores, and clearly call for a systematic check of the dycore non-physical contributions in the AAM budget for any GCM simulation of a superrotating atmosphere. The evaluation of ϵ (or ϵ^*) can be done through Eq. (7) and compared to T and F as done in our work.

Once these non-physical contributions have been identified in the AAM budget of a dycore and the quality of its conservation assessed, it is a difficult task to recommend any specific way to improve that problem. The LMD dycore is designed to conserve both potential enstrophy for barotropic nondivergent flows, and total angular momentum for axisymmetric flow. This implementation improved the angular momentum conservation properties of the model, as mentioned in *Hourdin et al.* [1995]. In the case of the CAM GCM, there are some parameters in the dycore (energy fixer, vertical mapping algorithm parameters) that could be played with to try to improve the situation. In physical height or pressure coordinates cyclic continuity guarantees that the pressure torque does not affect globally integrated AAM (except through mountain torque). This is not the case in sigma and hybrid coordinates. An area where sigma/hybrid coordinates can be especially problematic is with respect to mountain torques when steep topography is present. In these situations errors in the pressure gradient force become significant because two large terms of opposite sign must be added [*Smagorinsky et al.*, 1967; *Mesinger and Janjic*, 1985]. Methods have been devised to deal with this defect of the sigma system [*Mesinger*, 1973; *Simmons and Burridge*, 1981], including methods based on finite volume (Green-Gauss) schemes where the pressure gradient force is discretized as the net normal force on a volume of air divided by its mass [*Lin*, 1997; *Bradley and Dowling*, 2012]. In general, being able to assess the horizontal dissipation and sponge layer contributions separately from the rest of the dycore is mandatory to help adjust these processes in the dycore and minimize their impact on the AAM budget. The impact of both the horizontal and vertical resolutions need to be investigated in more details.

Acknowledgments. Work on this project was performed under the auspices of the Office of Science, US Department of Energy, by Lawrence Livermore National Laboratory under Contract DE-AC52-07NA27344, and was supported by NASA under grant NNX11AD67G. RLW was supported by NASA Grant NNX11AH82G. Authors thank Howard Houben for useful discussions.

References

Boer, G. J. (1990), Earth-atmosphere exchange of angular momentum simulated in a General Circulation Model and implications for the length of day, *J. Geophys. Res.*, *95*, 5511–5531, doi:10.1029/JD095iD05p05511.

Bradley, M. E., and T. E. Dowling (2012), Using 3D finite volume for the pressure-gradient force in atmospheric models, *Quart. J. Royal Met. Soc.*, doi:10.1002/qj.1929.

Collins, W. D., et al. (2004), Description of the NCAR Community Atmosphere Model (CAM 3.0), Tech. rep., National Center for Atmospheric Research, Boulder, CO, Technical Report NCAR/TN-464+STR.

Collins, W. D., et al. (2006), The Formulation and Atmospheric Simulation of the Community Atmosphere Model Version 3 (CAM3), *J. of Climate*, *19*, 2144–2161, doi: 10.1175/JCLI3760.1.

Del Genio, A. D., and W. Zhou (1996), Simulations of superrotation on slowly rotation planets: Sensitivity to rotation and initial conditions, *Icarus*, *120*, 332–343.

Egger, J., K. Weickmann, and K.-P. Hoinka (2007), Angular momentum in the global atmospheric circulation, *Rev. Geophys.*, *45*, RG4007, doi:10.1029/2006RG000213.

Friedson, A. J., R. A. West, E. H. Wilson, F. Oyafuso, and G. S. Orton (2009), A global climate model of Titan's atmosphere and surface, *Planet. & Space Sci.*, *57*, 1931–1949, doi:10.1016/j.pss.2009.05.006.

Held, I. M., and M. J. Suarez (1994), A Proposal for the Intercomparison of the Dynamical Cores of Atmospheric General Circulation Models, *Bull. Amer. Meteo. Soc.*, *75*, 1825–1830, doi:10.1175/1520-0477(1994)075<1825:APFTIO>2.0.CO;2.

Herrnstein, A., and T. E. Dowling (2007), Effect of topography on the spin-up of a Venus atmospheric model, *J. Geophys. Res.*, *112*, E04S08, doi:10.1029/2006JE002804.

Holton, J. R. (2004), *An introduction to dynamic meteorology*, International geophysics series, Amsterdam: Elsevier/Academic Press, 4th ed.

Hourdin, F., O. Talagrand, R. Sadourny, R. Courtin, D. Gautier, and C. P. McKay (1995), Numerical simulation of the general circulation of the atmosphere of Titan, *Icarus*, *117*, 358–374.

Hourdin, F., F. Couvreux, and L. Menut (2002), Parameterization of the dry convective boundary layer based on a mass flux representation of thermals, *J. of Atm. Sci.*, *59*, 1105–1123.

Jablonowski, C., and D. L. Williamson (2011), The pros and cons of diffusion, filters and fixers in atmospheric general circulation models, in *Numerical Techniques for Global Atmospheric Models*, *Lecture Notes in Computational Science and Engineering*, vol. 80, edited by P. H. Lauritzen, C. Jablonowski, M. A. Taylor, and R. D. Nair, pp. 381–493, Springer.

Lauritzen, P. H., A. A. Mirin, J. Truesdale, K. Raeder, J. L. Anderson, J. Bacmeister, and R. B. Neale (2012), Implementation of new diffusion/filtering operators in the CAM-FV dynamical core, *Int. J. High Perform. Comp. Appl.*, *26*, 63–73, doi:10.1177/1094342011410088.

Lebonnois, S., F. Hourdin, V. Eymet, A. Crespin, R. Fournier, and F. Forget (2010), Superrotation of Venus' atmosphere analysed with a full General Circulation Model, *J. Geophys. Res.*, *115*, E06,006, doi:10.1029/2009JE003458.

Lebonnois, S., J. Burgalat, P. Rannou, and B. Charnay (2012a), Titan Global Climate Model: new 3-dimensional version of the IPSL Titan GCM, *Icarus*, *218*, 707–722, doi:10.1016/j.icarus.2011.11.032.

Lebonnois, S., et al. (2012b), A comparative analysis of simplified general circulation models of Venus atmosphere, in *Towards understanding the climate of Venus: Application of terrestrial models to our sister planet*, edited by Bengtsson, L., Bonnet, R.-M., Grinspoon, D., Koumoutsaris, S., Lebonnois, S. and Titov, D., pp. –, Springer Netherlands, in press.

Lee, C. (2006), Modelling of the atmosphere of Venus, Ph.D. thesis, University of Oxford.

Lee, C., and M. I. Richardson (2010), A General Circulation Model ensemble study of the atmospheric circulation of Venus, *J. Geophys. Res.*, *115*, E04,002, doi:10.1029/2009JE003490.

Lee, C., S. R. Lewis, and P. L. Read (2007), Superrotation in a Venus general circulation model, *J. Geophys. Res.*, *112*, E04S11, doi:10.1029/2006JE002874.

Lejenäs, H., R. A. Madden, and J. J. Hack (1997), Global atmospheric angular momentum and Earth-atmosphere exchange of angular momentum simulated in a general circulation model, *J. Geophys. Res.*, *102*, 1931–1942, doi:10.1029/96JD03264.

Lin, S.-J. (1997), A finite-volume integration method for computing pressure gradient force in general vertical coordinates, *Quart. J. Royal Met. Soc.*, *123*, doi:10.1002/qj.49712354214.

Lin, S.-J. (2004), A "Vertically Lagrangian" Finite-Volume Dynamical Core for Global Models, *Mon. Weather Rev.*, *132*, 2293–2307, doi:10.1175/1520-0493(2004)132<2293:AVLFDC>2.0.CO;2.

Mellor, G. L., and T. Yamada (1982), Development of a turbulent closure model for geophysical fluid problems, *Rev. Geophys. Space Phys.*, *20*, 851–875.

Mesinger, F. (1973), A method for construction of second-order accuracy difference schemes permitting no false two-grid-interval wave in the height field, *Tellus*, *25*, 444–458.

Mesinger, F., and Z. I. Janjic (1985), Problems and numerical methods of the incorporation of mountains in atmospheric models, in *Large Scale Computations in Fluid Mechanics, Vol. 22, Part 2, Lectures in Applied Mathematics*, edited by B. E. Engquist, S. Osher and R. C. J. Somerville, American Mathematical Society, Providence, Rhodes Island.

Neale, R. B., et al. (2010), Description of the NCAR Community Atmosphere Model (CAM 5.0), National Center for Atmospheric Research, Boulder, CO, Technical Note.

Newman, C. E., C. Lee, Y. Lian, M. I. Richardson, and A. D. Toigo (2011), Stratospheric superrotation in the TitanWRF model, *Icarus*, *213*, 636–654, doi:10.1016/j.icarus.2011.03.025.

Parish, H. F., G. Schubert, C. Covey, R. L. Walterscheid, A. Grossman, and S. Lebonnois (2011), Decadal variations in a Venus General Circulation Model, *Icarus*, *212*, 42–65, doi:10.1016/ j.icarus.2010.11.015.

Richardson, M. I., A. D. Toigo, and C. E. Newman (2007), PlanetWRF: A general purpose, local to global numerical model for planetary atmospheric and climate dynamics, *J. Geophys. Res.*, *112*(E9), E09,001, doi:10.1029/2006JE002825.

Simmons, A. J., and D. M. Burridge (1981), An Energy and Angular-Momentum Conserving Vertical Finite-Difference Scheme and Hybrid Vertical Coordinates, *Mon. Weather Rev.*, *109*, 758–766, doi:10.1175/1520-0493(1981)109<0758:AEAAMC>2.0.CO;2.

Smagorinsky, J., L. Holloway, Jr., and G. D. Hembree (1967), Prediction experiments with a general circulation model, in *Proc. Inter. Symp. Dynamics Large Scale Atmospheric Processes*, pp. 70–134, Nauka, Moscow, U.S.S.R.

Tokano, T. (2012), Mountain torque and its influence on the atmospheric angular momentum on Titan, *Icarus*, *220*, 863–876, doi:10.1016/j.icarus.2012.06.027.

Tokano, T., F. M. Neubauer, M. Laube, and C. P. McKay (1999), Seasonal variation of Titan's atmospheric structure simulated by a general circulation model, *Planet. & Space Sci.*, *47*, 493–520.

Whitehead, J., C. Jablonowski, R. B. Rood, and P. H. Lauritzen (2011), A stability analysis of divergence damping on a latitude-longitude grid, *Mon. Weather Rev.*, *139*, 2976–2993.

Laboratoire de Météorologie Dynamique, IPSL, CNRS/UPMC, 4 place Jussieu, Box 99, F-75252 Paris Cedex 05, France

Table 1. Summary of simulation characteristics

Label	Initial state[a]	Topography	Radiative forcing[b]	Horiz. dissipation[c]	Duration[d]
Venus (LMD)					
LMDIN	Rest	no	NC	LEB10	400 Vd
LMDIT	Rest	yes	NC	LEB10	400 Vd
LMDFN	SR	no	Full RT	LEB10	50 Vd
LMDFT	SR	yes	Full RT	LEB10	50 Vd
Venus (CAM)					
IN2S	SR	no	NC	Default 2^{nd} order DD	150 Vd
IN4S	SR	no	NC	Default 4^{th} order DD	150 Vd
IN4R10	SR	no	NC	4^{th} order DD^d /10	150 Vd
IN4R30	SR	no	NC	4^{th} order DD^d /30	150 Vd
IN42R10	SR	no	NC	4^{th} order DD^d /10 +LD	150 Vd
I0N42R10	Rest	no	NC	4^{th} order DD^d /10 +LD	300 Vd
IT2S	SR	yes	NC	Default 2^{nd} order DD	150 Vd
IT4S	SR	yes	NC	Default 4^{th} order DD	150 Vd
IT4R10	SR	yes	NC	4^{th} order DD^d /10	150 Vd
IT4R30	SR	yes	NC	4^{th} order DD^d /30	150 Vd
IT42R10	SR	yes	NC	4^{th} order DD^d /10 +LD	150 Vd
I0T42R10	Rest	yes	NC	4^{th} order DD^d /10 +LD	100 Vd
Titan (LMD)					
TITAN	SR	no	Full RT	LEB12	1 Ty
Earth (CAM)					
EIN2S	Rest	no	HS	Default 2^{nd} order DD	10 Ey
EIN4S	Rest	no	HS	Default 4^{th} order DD	10 Ey
EIN4R10	Rest	no	HS	4^{th} order DD^d /10	10 Ey

[a]: SR = Already in superrotation
[b]: NC = Newtonian Cooling; HS = Held-Suarez [*Held and Suarez*, 1994]
[c]: LEB10 = *Lebonnois et al.* [2010]; LEB12 = *Lebonnois et al.* [2012a]; DD = divergence damping [*Lauritzen et al.*, 2012]; LD = additional Laplacian damping at the top
[d]: Vd = Venus day (1×10^7 s); Ty = Titan year (9.3×10^8 s); Ey = Earth year (3.1×10^7 s)

Table 2. Temporal average values of the torques in the different simulations. Units are 10^{18} kg m^2 s^{-2} for Venus and the Earth, 10^{15} kg m^2 s^{-2} for Titan.

	$\overline{dM_r/dt}$	$\overline{\Sigma}$	$\overline{T}$	$\overline{F}$	$\overline{D}$	$\overline{S}$	$\overline{\epsilon}$	$\overline{\epsilon^*}$
LMDIN	2.71	2.69	0.	9.49	-1.57	-0.02	-5.20	-6.79
LMDIT	1.10	1.09	-1.72	1.57	-0.28	-0.02	1.54	1.24
LMDFN	-1.09	-1.08	0.	-0.43	0.15	-0.05	-0.76	-0.66
LMDFT	0.11	0.11	0.62	-4.04	-0.32	-0.08	3.94	3.54
IN2S	-5.88	-5.85	0.	0.70				-6.54
IN4S	-3.41	-3.39	0.	1.74				-5.13
IN4R10	-0.83	-0.82	0.	-0.07				-0.75
IN4R30	-1.73	-1.72	0.	-0.66				-1.06
IN42R10	-1.53	-1.52	0.	-0.19				-1.32
I0N42R10	4.58	4.54	0.	0.47				4.07
IT2S	1.29	1.28	32.12	0.10				-30.92
IT4S	2.02	2.01	-114.54	0.17				116.52
IT4R10	3.69	3.66	0.36	0.16				3.18
IT4R30	3.50	3.47	18.42	0.16				-15.08
IT42R10	3.51	3.47	-5.87	0.16				9.23
I0T42R10	3.86	3.83	0.53	0.15				3.19
TITAN	2.83	2.80	0.	9.43	-2.59	-1.34	-2.70	-6.63
EIN2S	0.34	-0.32	0.	11.06				-11.33
EIN4S	0.08	-0.59	0.	11.04				-11.60
EIN4R10	0.13	-0.57	0.	17.54				-18.17

Table 3. Temporal average values of the competitive positive and negative surface torques in the different simulations, compared to $\overline{\epsilon^*}$. The dimensionless ratio ξ is defined in the text. Units (other than ξ) are 10^{18} kg m^2 s^{-2} for Venus and the Earth, 10^{15} kg m^2 s^{-2} for Titan.

	$\overline{T^+}$	$\overline{T^-}$	$\overline{F^+}$	$\overline{F^-}$	$\overline{\epsilon^*}$	ξ
LMDIN	0.	0.	10.23	-0.74	-6.79	0.66
LMDIT	28.13	-29.86	4.83	-3.26	1.24	0.04
LMDFN	0.	0.	0.50	-0.94	-0.66	0.70
LMDFT	30.73	-30.09	2.19	-6.24	3.54	0.10
IN2S	0.	0.	0.94	-0.24	-6.54	6.96
IN4S	0.	0.	1.74	-0.	-5.13	2.95
IN4R10	0.	0.	0.26	-0.33	-0.75	2.27
IN4R30	0.	0.	0.13	-0.79	-1.06	1.34
IN42R10	0.	0.	0.24	-0.43	-1.32	3.07
I0N42R10	0.	0.	0.59	-0.12	4.07	6.90
IT2S	273.9	-241.6	0.17	-0.07	-30.92	0.11
IT4S	216.1	-330.6	0.23	-0.06	116.52	0.35
IT4R10	267.5	-267.1	0.23	-0.07	3.18	0.01
IT4R30	274.2	-255.8	0.23	-0.07	-15.08	0.05
IT42R10	263.9	-269.8	0.23	-0.07	9.23	0.03
I0T42R10	265.0	-264.5	0.22	-0.07	3.19	0.01
TITAN	0.	0.	34.3	-24.9	-6.63	0.19
EIN2S	0.	0.	98.8	-87.8	-11.33	0.12
EIN4S	0.	0.	101.4	-90.3	-11.60	0.11
EIN4R10	0.	0.	102.7	-85.2	-18.17	0.18

Table 4. Summary of the different variables used in Section 3.

Notation	Description
M	Total atmospheric angular momentum (AAM)
M_o	Solid-body rotation part of M, due to planetary rotation Ω
M_r	Relative part of M, due to zonal wind u
F	Surface torque on the atmosphere due to friction
T	Mountain torque on the atmosphere due to topography
S	Torque on the atmosphere due to upper boundary conditions (sponge layer)
D	Residual torque due to conservation errors in the horizontal dissipation parameterization
Dy	Total variation of AAM in the dycore of the GCM
ϵ	Residual numerical rate of AAM variation due to conservation errors in the dycore
ϵ^*	$= S + D + \epsilon$, should theoretically be zero
Σ	$= F + Dy$, should be equal to dM_r/dt
F^+	Positive (source) part of the friction torque
F^-	Negative (sink) part of the friction torque
T^+	Positive (source) part of the mountain torque
T^-	Negative (sink) part of the mountain torque
ξ	Ratio between $\lvert\overline{\epsilon^*}\rvert$ and $Max\left(\overline{T^+} + \overline{F^+}, \lvert\overline{T^-} + \overline{F^-}\rvert\right)$

The overbar indicates a time average over the whole simulation.

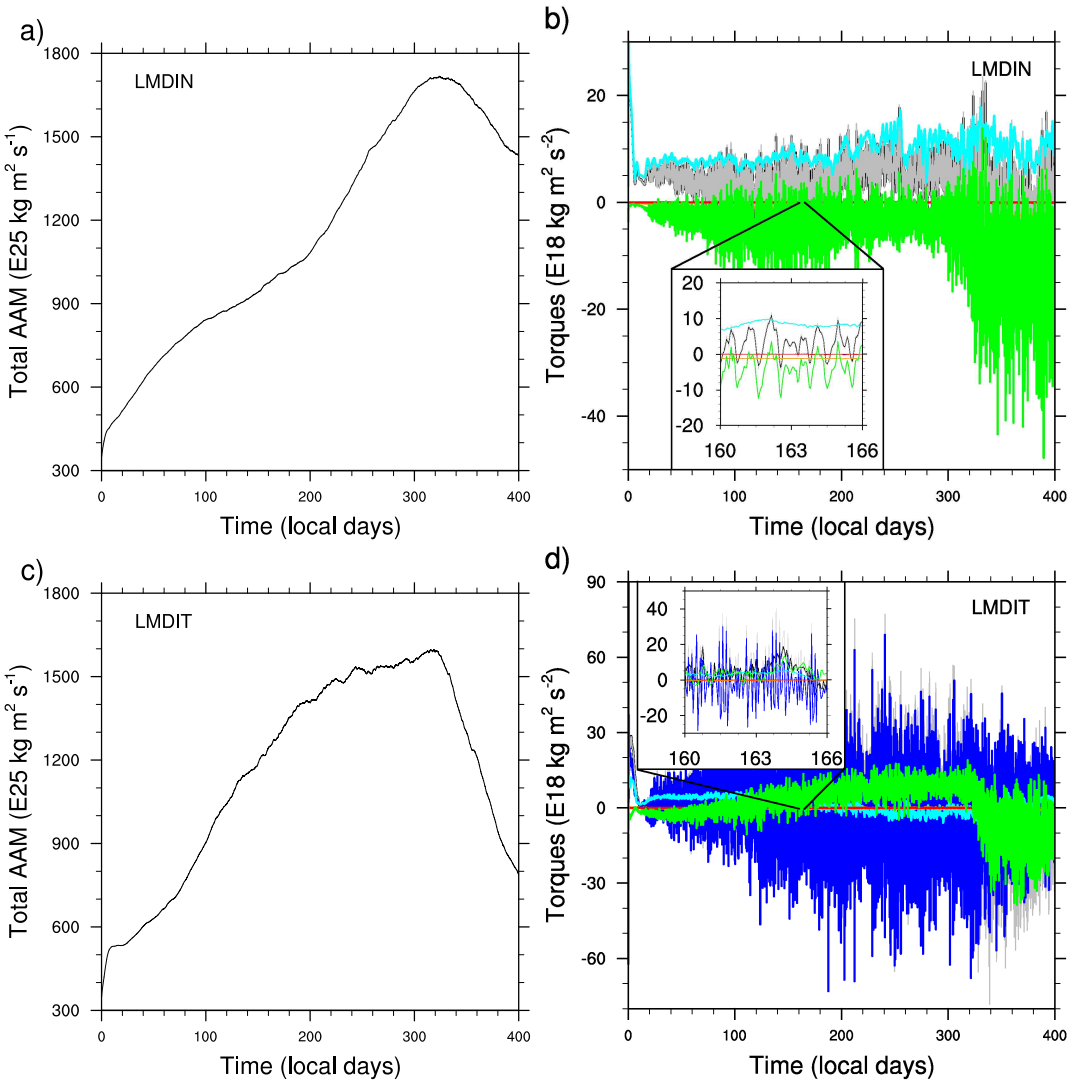

Figure 1. LMD idealized physics simulations: First row without topography (LMDIN), second row with topography (LMDIT); first column: M. The color scheme for the torques is: black: dM_r/dt (computed as a temporal centered difference from M_r); gray: $\Sigma = F + Dy$; light blue: surface friction F; blue: mountain torque T; orange: horizontal dissipation D; red: sponge layer S; green: residual from dynamics ϵ.

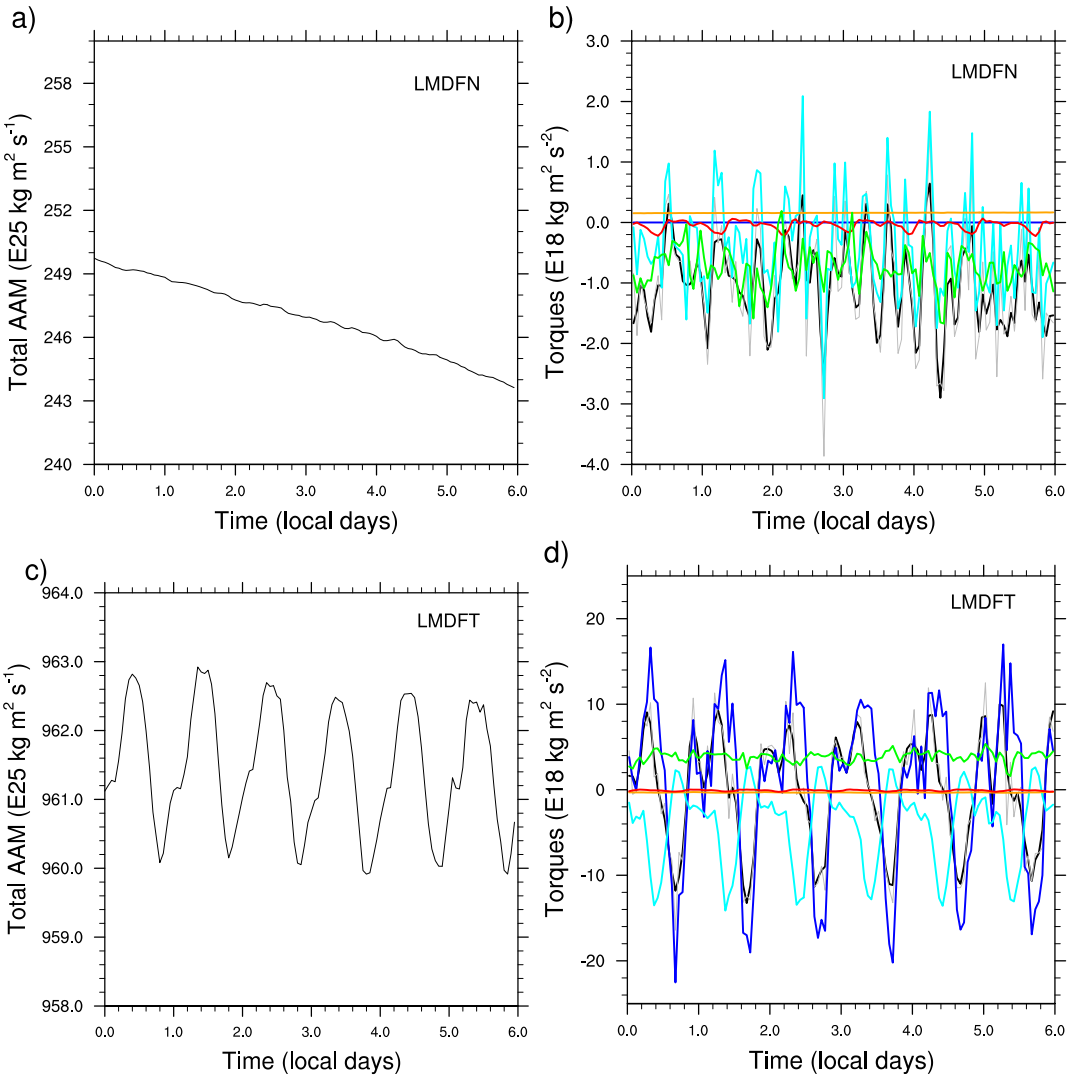

Figure 2. LMD full physics simulations: First row without topography (LMDFN), second row with topography (LMDFT); first column: M. Torques color scheme: black: dM_r/dt; gray: Σ; light blue: F; blue: T; orange: D; red: S; green: ϵ. For clarity purposes, only 6 Venus days taken from our simulations are plotted.

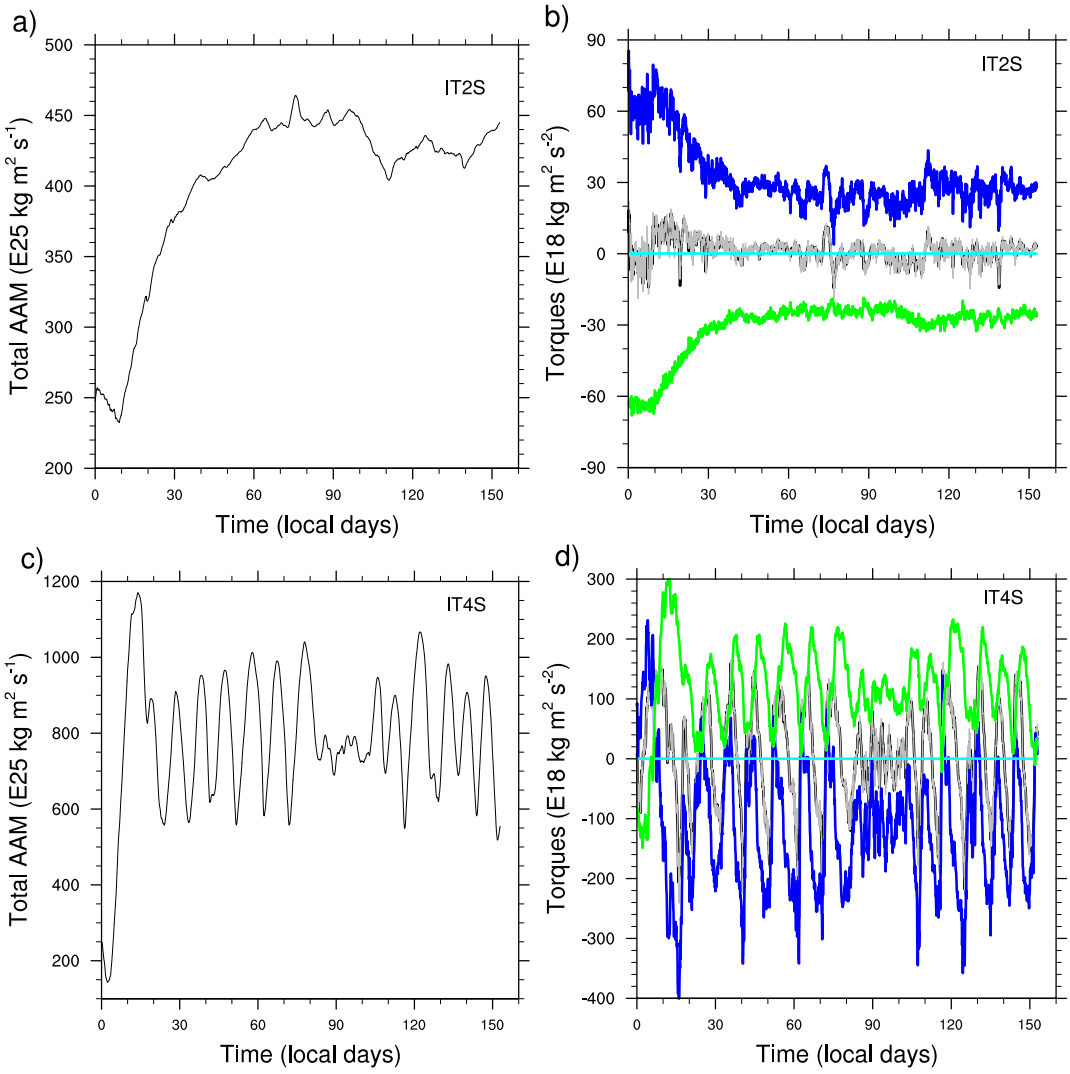

Figure 3. CAM5 simulations with 2nd-order (first row, IT2S) and 4th-order (second row, IT4S) divergence damping; first column: M. The torques color scheme is the same as Fig. 1, except that green is ϵ^*: black: dM_r/dt; gray: Σ; light blue: F; blue: T; green: ϵ^*.

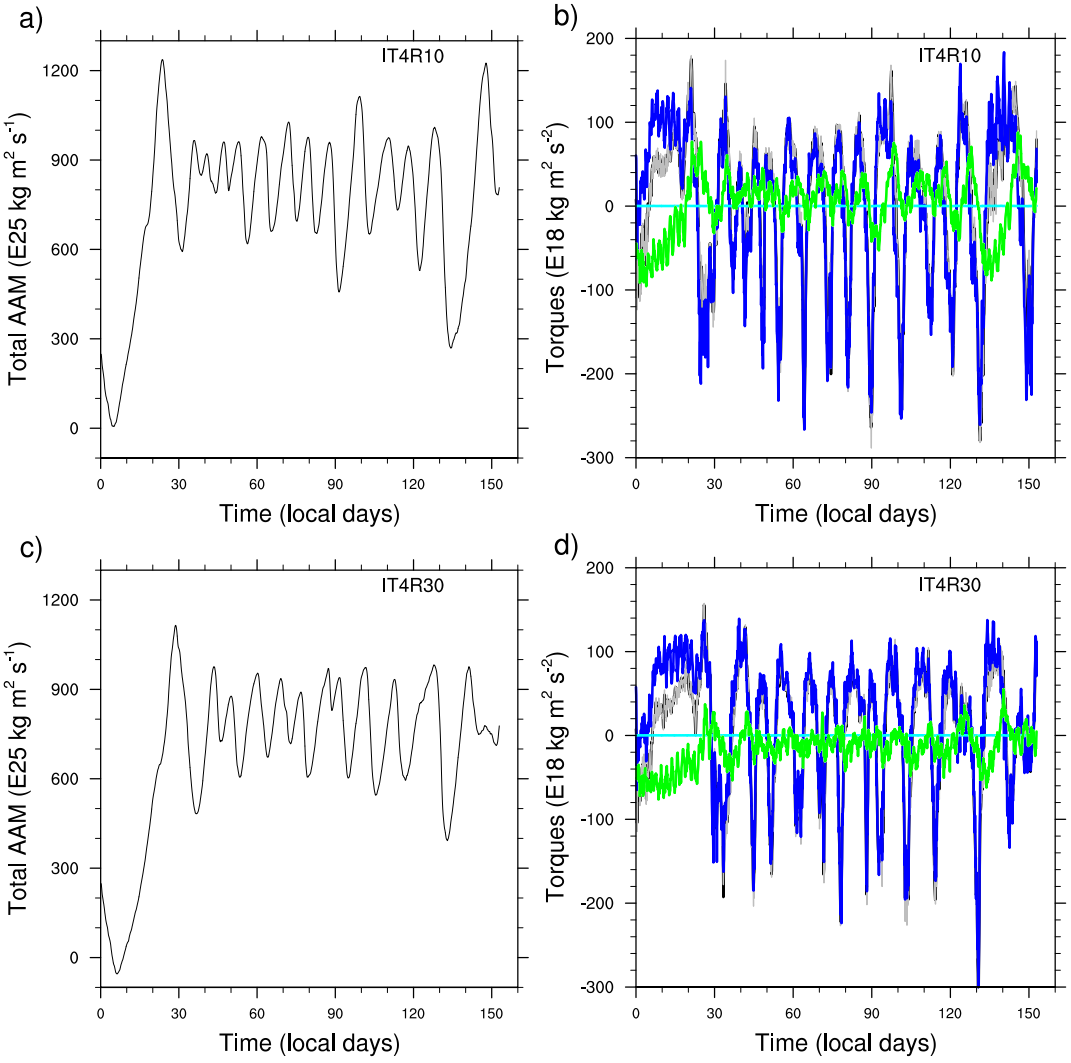

Figure 4. Same as Fig. 3, but with a reduced coefficient for the 4th-order divergence damping. First row is IT4R10, second is IT4R30. Torques color scheme: black: dM_r/dt; gray: Σ; light blue: F; blue: T; green: ϵ^*.

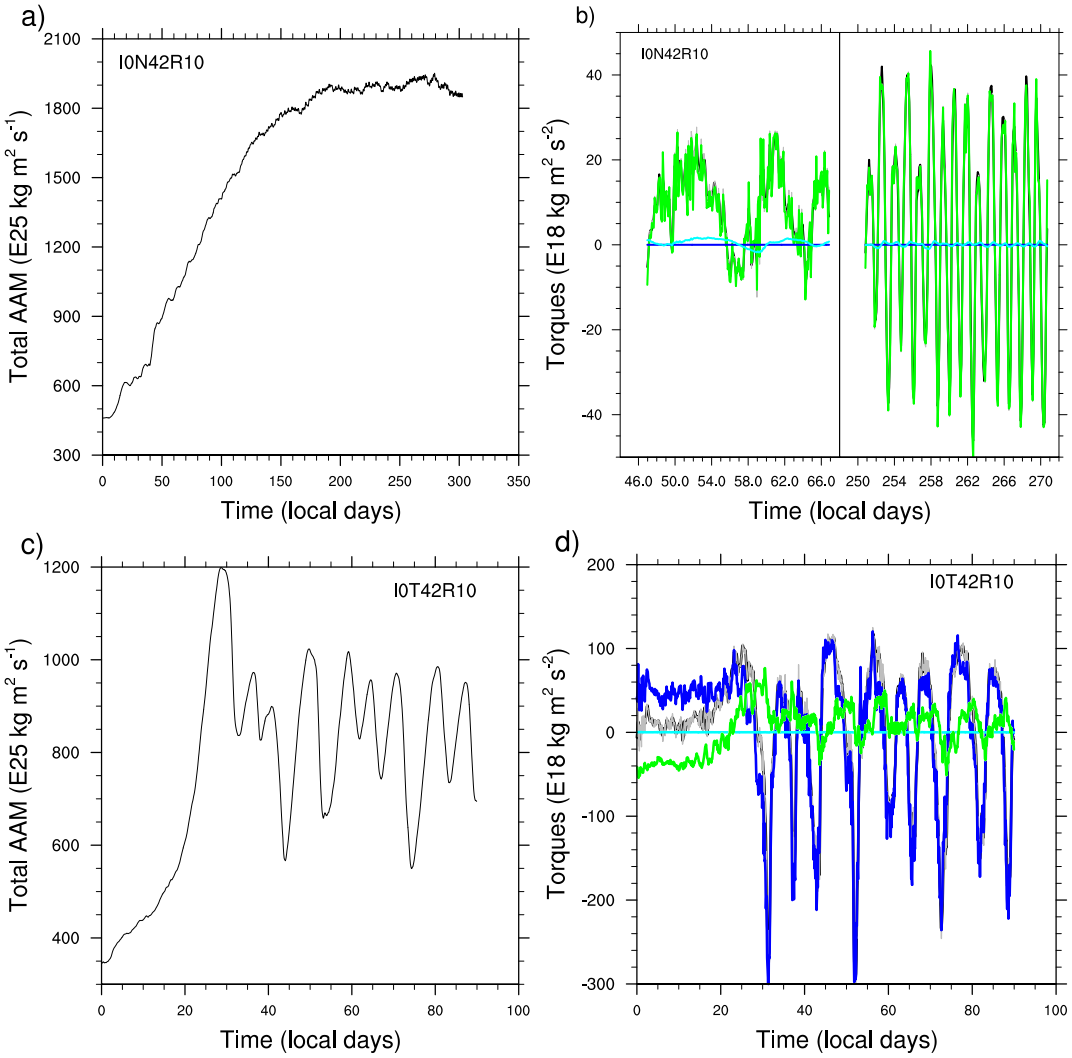

Figure 5. Same as Fig. 3, but starting from initial rest, without topography (first row, I0N42R10) and with topography (second row, I0T42R10). For readability, two periods of 20 Vd are plotted for the I0N42R10 torques: during spin-up and during steady state. Torques color scheme: black: dM_r/dt; gray: Σ; light blue: F; blue: T; green: ϵ^*.

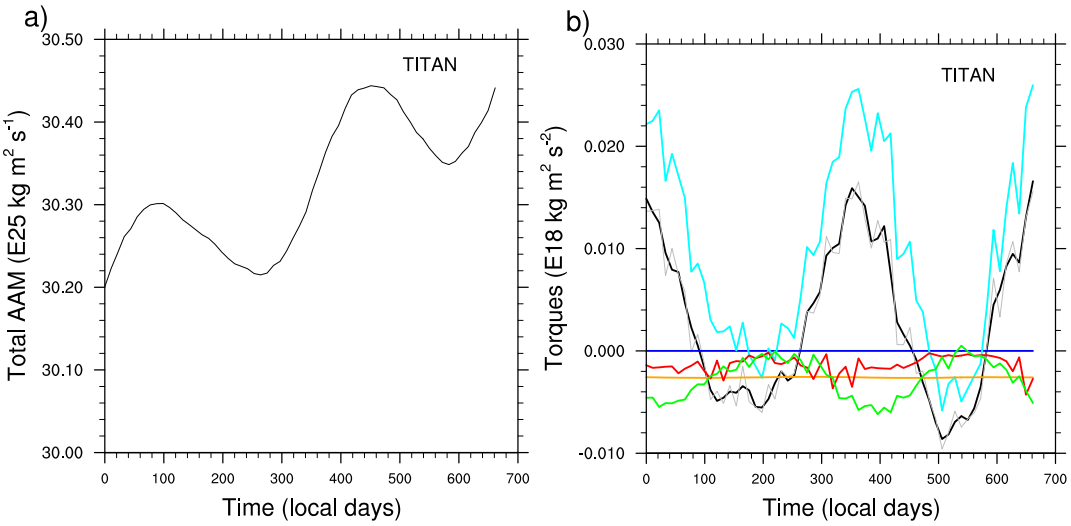

Figure 6. LMD Titan simulation, (a) is M. One Titan year is shown, starting at northern spring equinox. Torques color scheme: black: dM_r/dt; gray: Σ; light blue: F; blue: T; orange: D; red: S; green: ϵ.

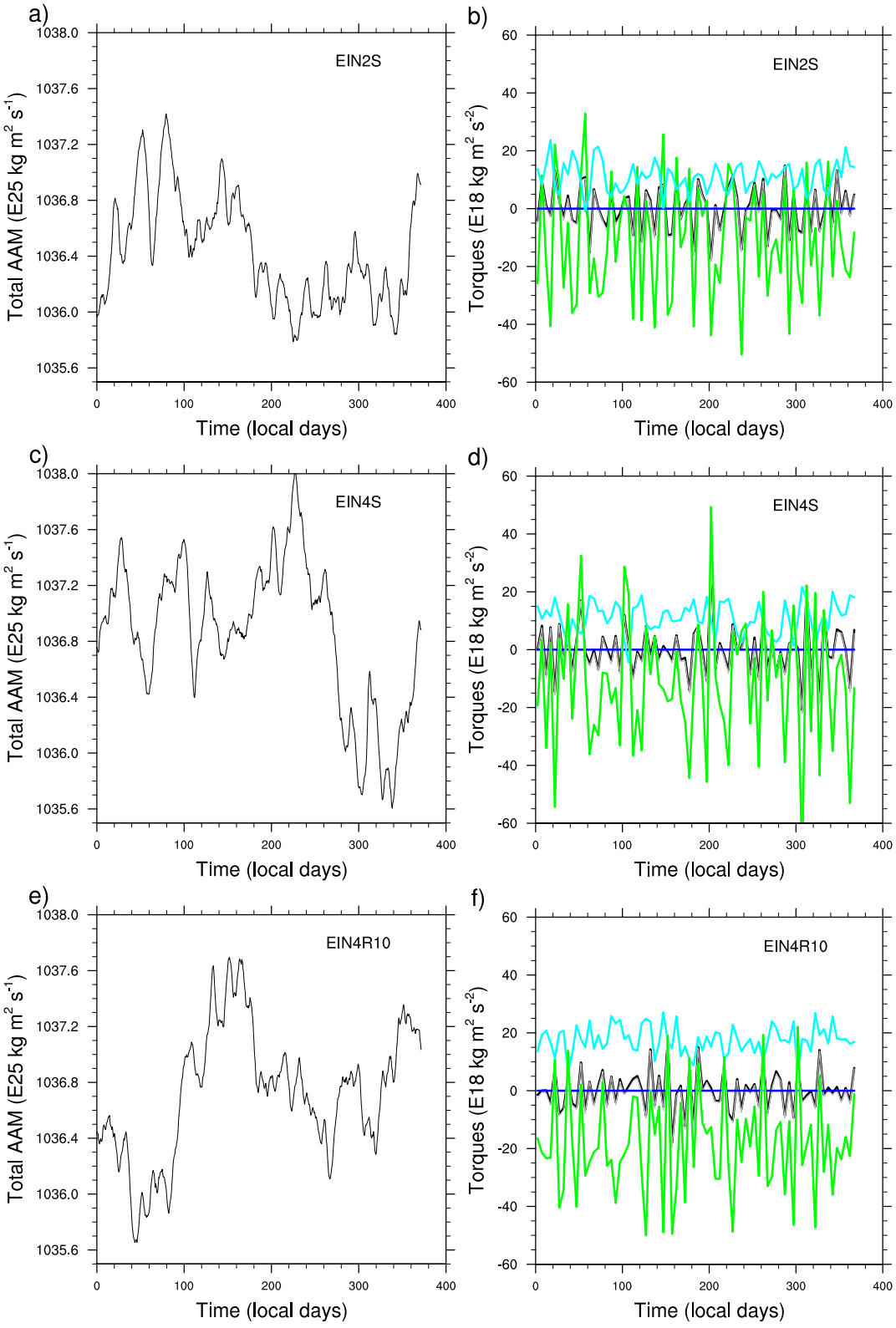

Figure 7. CAM5 simulations for Earth Held-Suarez configuration, 10th year. First row is with 2nd-order divergence damping (EIN2S), second row with 4th-order divergence damping (EIN4S) and third row for 4th-order divergence damping with reduced (1/10) coefficient (EIN4R10). First column: M. Torques color scheme: black: dM_r/dt; gray: Σ; light blue: F; blue: T; green: ϵ^*.